1D AND 2D NMR CORE-LOG INTEGRATION IN ORGANIC SHALE

Philip M. Singer, Erik Rylander, Tianmin Jiang, Ryan McLin, Richard E. Lewis, Schlumberger, Steven M. Sinclair, Matador Resources Company

This paper was prepared for presentation at the International Symposium of the Society of Core Analysts held in Napa Valley, California, USA, 16-19 September, 2013.

ABSTRACT

Production of oil and gas from organic shale is a function of porosity, hydrocarbon saturation, pore pressure, matrix permeability, hydraulic fracture surface area, and fracture conductivity. Hydraulic fracture surface area, porosity, saturations and pore pressure dominate initial production rates, while matrix permeability becomes increasingly important in sustaining production later in time. Permeability measurements to oil from organic shale core samples are not commercially available today. However, permeability to oil is believed to be a function of effective porosity, pore throat size, wettability, and water saturation, similar to conventional reservoirs. This work investigates pore size, fluid saturation, wettability, and expelled hydrocarbon volumes using log and core-based nuclear magnetic resonance (NMR) data from oil-bearing shale in the lower Eagle Ford. Tight Rock Analysis (TRA) core porosities, scanning electron microscope (SEM) images, and mercury injection capillary pressure (MICP) measurements are compared with NMR interpretation for calibration and validation.

INTRODUCTION

The use of NMR logging for formation evaluation in unconventional reservoirs has demonstrate considerable promise in recent years [1-6], including the interpretation of 1D (1-dimensional) NMR and 2D (2-dimensional) NMR data. As with all new log interpretation techniques, the parameters used to analyze the logs have to be calibrated and validated with core data for more accurate reservoir characterization. Ideally, core analysis on these unconventional reservoir rocks [7-10] should be performed whenever logs are first introduced in exploration wells. For example, the traditional $T_{2\text{cutoff}}$ for movable fluid in oil-bearing shale formations is significantly different from conventional sandstone and carbonate reservoirs [5,6]. Using a properly calibrated $T_{2\text{cutoff}}$ in NMR log interpretation yields more accurate reserve estimates and more accurate identification of producible target zones. Understanding which portion of a shale reservoir contains producible fluids impacts target zone selection and ultimate recovery.

The rest of this report is organized as follows: (1) experimental details, (2) calibration of log-NMR data for movable fluid and effective fluid porosity, which is achieved by integrating log-NMR data with core-NMR, TRA, and MICP porosity, (3) calibration of 2D core-NMR data for interpreting fluid types and fluid porosities, which is achieved by integrating TRA data with core-NMR data, (4) temperature dependence of the separate fluid phases from 2D core-NMR data, and, (5) calibration of the pore-body size from log-

NMR data, which is achieved by integrating log-NMR data with SEM images. The last section also investigates a matrix permeability model which utilizes the MICP data.

EXPERIMENTAL

Ten 1.5 inch × 2.0 inch core-plugs spaced every 10 feet across the lower Eagle Ford Shale were picked to avoid any high clay streaks. Core-NMR, SEM, MICP, core porosity, and core permeability measurements were performed at each sampled depth. Measurements on the core-plugs began about 14 months after the core was recovered. The bulk densities had not changed, indicating good core preservation over the 14 month period. The well was drilled with oil based mud, which adds uncertainty in the comparison between core and log saturations.

The core-NMR data were acquired on a GeoSpec2 rock-core analyzer from Oxford Instruments. Both the resonance frequency of 2.4 MHz and the inter-echo spacing of T_E = 0.2 ms for the core NMR were similar to the log NMR. The core-NMR data were measured at ambient temperature (22 °C) and at reservoir temperature (100 °C) using a specially designed core-holder. A pore pressure of 200 psi was maintained with nitrogen gas in order to maintain the liquid phase of the saturating fluids in the core during heating. No confining stress was applied. The NMR response of the core samples before and after heating did not change, indicating that the core samples were not altered by the heating. Core-NMR T_1-T_2 maps were acquired with T_E = 0.2 ms and 24 log-spaced inversion recovery steps ranging from 0.2 ms ⇔ 1000 ms.

MICP was measured using a Micromeritics AutoPore IV 9520 mercury porosimeter. The samples were dried in a vacuum oven at 90 °C for 24 hours, and were then broken into pieces small enough to fit within the glass penetrometers. A vacuum of 50 μTorr was pulled on the sample, followed by mercury injection at multiple pressures up to 60,000 psi. For SEM sample preparation, the shale core samples were broken open perpendicular to bedding to expose a fresh surface similar to a fracture face in the subsurface, and then coated with a thin conductive coating of platinum-palladium. The samples were then examined in secondary electron mode with an FEI Quanta 400F scanning electron microscope equipped with an EDAX energy dispersive X-ray unit for spectral analysis.

Core porosity measurements were conducted using thermal extraction by TRA retort [11]. The following equations are assumed for calibrating the NMR porosities (left hand side) with the TRA fluid porosities (right hand side):

$$\varphi_{\mathrm{LogNMR}^2} = \varphi_{\mathrm{g}} + \varphi_{\mathrm{o2}} + \varphi_{\mathrm{o3}} + \varphi_{\mathrm{w1}} + \varphi_{\mathrm{w2}} \quad (1)$$

$$\varphi_{\mathrm{CoreNMR}^2} = \varphi_{\mathrm{o2}} + \varphi_{\mathrm{o3}} + \varphi_{\mathrm{w1}} + \varphi_{\mathrm{w2}} \quad (2)$$

$$\varphi_{\mathrm{CoreNMR}^1} = \varphi_{\mathrm{o2}} + \varphi_{\mathrm{o3}} + \varphi_{\mathrm{w1}} + \varphi_{\mathrm{w2}} + \varphi_{\mathrm{w3}} \quad (3)$$

$$\varphi_{\mathrm{Effective}} = \varphi_{\mathrm{g}} + \varphi_{\mathrm{o2}} + \varphi_{\mathrm{w1}} \quad (4)$$

The TRA fluids are defined as φ_{g} for gas filled porosity, φ_{w1} for water porosity at retort temperature #1 (121 ^{o}C), φ_{w2} for water porosity at retort temperature #2 (316 ^{o}C), φ_{w3} for water porosity at retort temperature #3 (704 ^{o}C), φ_{o2} for hydrocarbon porosity at retort temperature #2, and, φ_{o3} for hydrocarbon porosity at retort temperature #3. At each stage, the retort temperature is held until the rock stops exuding fluid. The log-NMR total porosity is defined as $\varphi_{\mathrm{LogNMR2}}$. The subscript "2" refers to processing the T_2 decay using the 2nd echo and beyond, which is done to eliminate any possible influence of tool ringing on the 1st echo. For the purposes of log-NMR calibration, the core-NMR total porosity $\varphi_{\mathrm{CoreNMR2}}$ likewise uses the 2nd echo and beyond. For calibrating fluid types from 2D core-NMR, the full T_2 decay including the 1st echo is used, and the total porosity is defined as $\varphi_{\mathrm{CoreNMR1}}$. The effective porosity is defined as $\varphi_{\mathrm{Effective}}$, which is taken directly from [11].

MOVABLE AND EFFECTIVE POROSITY FROM 1D NMR

Having a movable-fluid porosity log together with an effective porosity log is paramount for reservoir characterization. The movable porosity provides the readily producible fluid porosity of the reservoir, while the effective porosity provides the ultimate recoverable porosity with a good fracture network. Having both porosity logs properly calibrated is crucial for accurate reserve estimates and for identifying target zones. Three of the ten core samples were centrifuged to air at an inlet capillary pressure of 1000 psi and a chamber temperature of 77 °C for 72 hours to remove any remaining moveable fluid. No fluids were produced after 72 hours of spinning to air, and core NMR confirmed no change in porosity or T_2 response. The null result suggests that the majority of the movable fluid escaped the core during core retrieval to surface. Assuming Darcy permeability and a resolution of 0.1 cm^3 for detecting produced fluids in the centrifuge device, an upper bound to the mobility of the remaining fluid in the core is estimated to be 2.5 nD/cP.

Given that no fluids were produced after centrifugation, it is reasonable to assume that the remaining porosity in the core is a good measure of the bound fluid porosity. Put in other words, the movable fluid porosity can be equated to the gas filled porosity φ_{g} with reasonable certainty. With this assertion, a cutoff defined as $T_{2,\text{cutoff-movable}}$ which separates movable from bound fluid in the log-NMR response is calibrated with core-NMR data. As stated in Eqs. (1) and (2), the movable fluid porosity φ_{g} is the difference between $\varphi_{\mathrm{LogNMR2}}$ and $\varphi_{\mathrm{CoreNMR2}}$. Fig. 1b illustrates how the partial log-NMR porosity below $T_2 < T_{2,\text{cutoff-movable}}$ is matched (i.e. calibrated) to $\varphi_{\mathrm{CoreNMR2}}$. The optimal calibration value $T_{2,\text{cutoff-movable}}$ = 8.3 ms is determined by minimizing the residual over all core depths as a function of $T_{2,\text{cutoff-movable}}$:

$$\text{Residual} = \sum_i \left(\varphi^i_{\mathrm{LogNMR2}}\left(T_2 < T_{2,\text{cutoff-movable}}\right) - \varphi^i_{\mathrm{CoreNMR2}}\right)^2 \qquad (5)$$

The summation index i is over the 10 core depths. It is interesting to note that the majority of the core-NMR signal in Fig. 1a is below $T_2 < T_{2,\text{cutoff-movable}}$, which is

consistent with the assertion that the core-NMR porosity is all bound fluid.

Fig. 2 shows the correlation analysis between the calibrated log-NMR movable fluid porosity and the independent TRA gas porosity. Fair agreement in the average values indicates that the above assumptions are reasonable. Also shown in Fig. 2 is the log-NMR total porosity versus the independent TRA total porosity in Eq. (1). Typically, a *p*-value of $p < 0.05$ indicates significant correlation in the paired dataset. If heterogeneity exists in the rock, some of the scattering in the data may be due to the different length scales of investigation between core-NMR (~2 inch) and log-NMR (~7 inch) data.

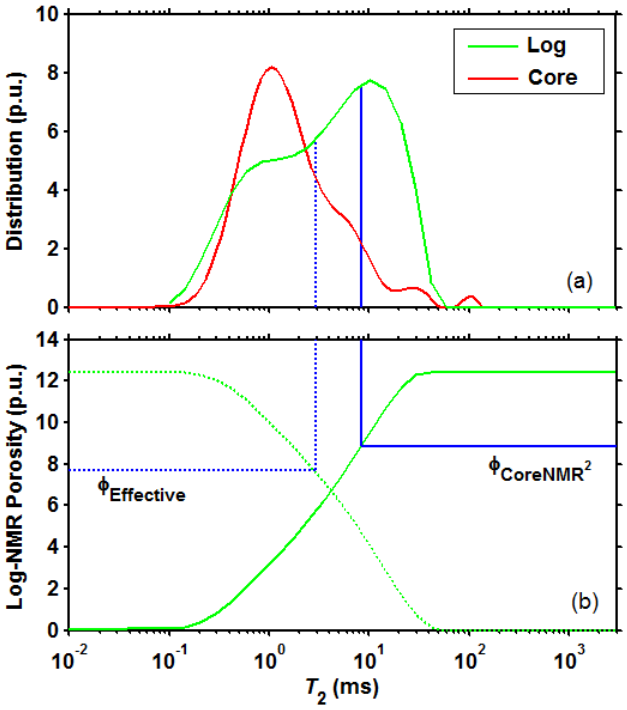

Fig. 1: Representative example of log-NMR calibration with core. (a) Log-NMR (green) and core-NMR (red) T_2 distribution at 100 °C. (b) Log-NMR distribution cumulated from the left (solid green), together with $T_{2,\text{cutoff-movable}}$ = 8.3 ms (solid blue) calibrated from the core-NMR total porosity $\varphi_{\text{CoreNMR}^2}$. Also shown is the log-NMR distribution cumulated from the right (dotted green), together with $T_{2,\text{cutoff-effective}}$ = 2.9 ms (dotted blue) calibrated from the TRA effective porosity $\varphi_{\text{Effective}}$.

Fig. 1b also shows an example of the calibration process where the cumulated log-NMR porosity above $T_2 > T_{2,\text{cutoff-effective}}$ is matched to the effective porosity from TRA data.

The optimal value $T_{2,\text{cutoff-effective}}$ = 2.9 ms from TRA is determined in a similar fashion to Eq. (5), where the residual is minimized over all core depths as a function of $T_{2,\text{cutoff-effective}}$:

$$\text{Residual} = \sum_i \left(\varphi^i_{\text{LogNMR}^2}\left(T_2 > T_{2,\text{cutoff-effective}}\right) - \varphi^i_{\text{Effective}}\right)^2 \quad (6)$$

The correlation from the calibration of effective porosity is presented in Fig. 3.

$T_{2,\text{cutoff-movable}}$ calibrated with Core-NMR	$T_{2,\text{cutoff-effective}}$ calibrated with TRA	$T_{2,\text{cutoff-effective}}$ calibrated with MICP
8.3 ms	2.9 ms	2.4 ms
219 nm	76 nm	63 nm

Table 1: List of log-NMR $T_{2,\text{cutoff}}$ parameters (first row) calibrated with various core data. Also listed is each $T_{2,\text{cutoff}}$ converted into pore-body diameter (second row), as discussed in the pore body and throat size section.

Similar analysis using MICP data yields a consistent value $T_{2,\text{cutoff-effective}}$ = 2.4 ms, where $\varphi_{\text{Effective}}$ in Eq. (6) is the MICP injected porosity instead. The MICP

measurement is performed after drying the samples and applying a high vacuum, which has the effect of removing all the effective water and effective oil. The mercury is then injected into all the effective porosity pore space, defined in Eq. (4).

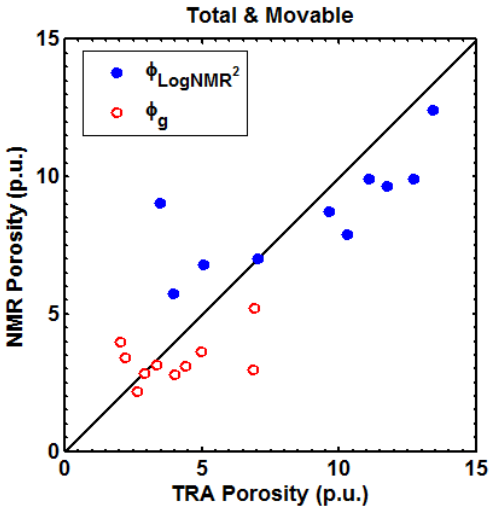

Fig. 2: Correlation cross-plot (filled blue) of the log-NMR total porosity $\varphi_{\mathrm{LogNMR^2}}$ versus the independent TRA total porosity, defined in Eq. (1). Also shown is the correlation cross-plot (open red) of log-NMR movable porosity where core-NMR data was used to calibrate $T_{2,\mathrm{cutoff\text{-}movable}}$ = 8.3 ms in Eq. (5), versus the independent TRA gas porosity φ_g. The correlation is: $\boldsymbol{R^2}$ **= 0.58** and $\boldsymbol{p}$ **= 0.010** for $\varphi_{\mathrm{LogNMR^2}}$; $\boldsymbol{R^2}$ **= 0.17** and $\boldsymbol{p}$ **= 0.24** for φ_g.

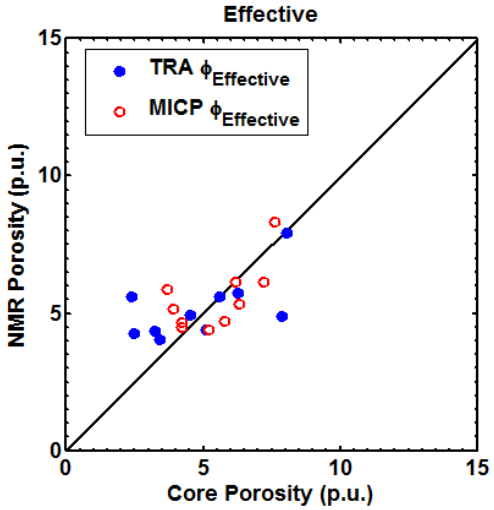

Fig. 3: Correlation cross-plot (filled blue) of the log-NMR effective porosity versus the TRA effective porosity, where TRA was used to calibrate $T_{2,\mathrm{cutoff\text{-}effective}}$ = 2.9 ms in Eq. (6). Also shown is the correlation cross-plot (open red) of the log-NMR $\varphi_{\mathrm{Effective}}$ versus the MICP effective porosity, where MICP was used to calibrate $T_{2,\mathrm{cutoff\text{-}effective}}$ = 2.4 ms in Eq. (6). The correlation is: $\boldsymbol{R^2}$ **= 0.37** and $\boldsymbol{p}$ **= 0.060** for TRA; $\boldsymbol{R^2}$ **= 0.42** and $\boldsymbol{p}$ **= 0.042** for MICP.

FLUID TYPING AND SATURATION FROM 2D NMR

With the producible fluids now quantified, the next task is to determine the fluid saturations. The fluid identification from core-NMR is performed with 2D T_1-T_2 mapping. The motivation for this analysis stems from A.E. Ozen *et al.* [10], where it was reported that organic shale cuttings saturated with oil had T_1/T_2 ratios up to two times greater than when saturated with water. Given this observation, a T_1/T_2 ratio cutoff is used which discriminates water from hydrocarbon in oil-bearing shale.

The core-NMR T_1-T_2 maps are partitioned into four quadrants: (1) φ_{o3}, (2) φ_{o2}, (3) φ_{w3}, and (4) φ_{w1+w2}. The term φ_{w1+w2} is equivalent to $\varphi_{w1}+\varphi_{w2}$. The φ_{w1} porosity was small compared to all others, and was therefore added to φ_{w2} in the analysis. The interpretation and terminology from Ref. [11] is as follows: (1) φ_{o3} is bound hydrocarbon which consists of bound oil and some bitumen, (2) φ_{o2} is total oil, a.k.a. effective oil, which includes capillary-bound oil in oil-wet inter-granular or intra-granular particle (IP) pores and organic matter (OM) pores [12], (3) φ_{w3} is structural clay-bound water, a.k.a. hydroxyls, and (4) φ_{w1+w2} is total water which consists of interstitial clay-bound water plus effective water, and includes capillary-bound water in water-wet IP pores.

The first task in calibrating core-NMR fluids from TRA data is to compare the total liquid porosity $\varphi_{\mathrm{CoreNMR1}}$ defined in Eq. (3). The gas filled porosity φ_{g} is not included since core NMR does not measure air (i.e. gas). Note, however, that the gas porosity can be derived from NMR data alone (see Fig. 2) using the movable fluid analysis. Fig. 4 shows a good correlation between the total core-NMR porosity $\varphi_{\mathrm{CoreNMR1}}$ at 100 °C and the independent TRA total liquid porosity. This implies that $\varphi_{\mathrm{CoreNMR1}}$ detects all the TRA liquid porosity (including all the clay-bound water), which thereby justifies the assumptions behind Eq. (3).

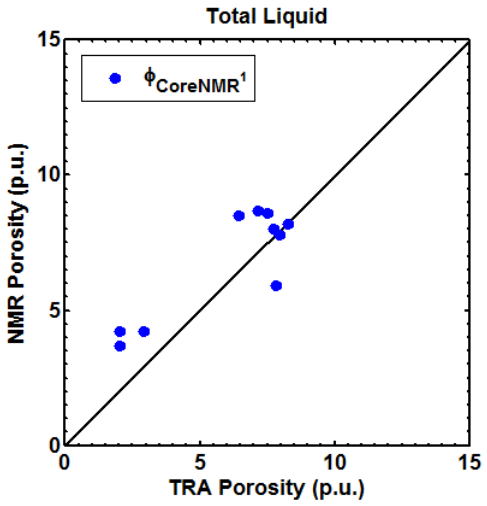

Fig. 4: Correlation cross-plot of the total core-NMR porosity $\varphi_{\mathrm{CoreNMR1}}$ at 100 °C versus the independent TRA total liquid porosity (filled blue), defined in Eq. (3). The correlation is: $\boldsymbol{R^2}$ = **0.77** and $\boldsymbol{p}$ = **0.001**.

The fluid component with the shortest T_2 is most likely φ_{w3}, which according to [11] is interpreted as structural clay-bound water. The fact that $\varphi_{\mathrm{CoreNMR1}}$ detects φ_{w3} at all suggests that there may be hydrogen exchange between solid clay-bound sites and the fluid-like capillary bound sites. It is surmised that the effect of dropping the 1st echo for both $\varphi_{\mathrm{LogNMR2}}$ and $\varphi_{\mathrm{CoreNMR2}}$ has the effect of dropping out φ_{w3} due to its short T_2. This assumption is validated in Fig. 2, where the total porosity $\varphi_{\mathrm{LogNMR2}}$ (which does *not* include φ_{w3}) shows a good correlation with the independent TRA porosity, thereby justifying Eq. (1).

The other fluid component with short T_2 is φ_{o3}, which consists of bound oil and viscous hydrocarbon such as bitumen. It is most likely that NMR is not able to detect all the bitumen porosity, however, the summation of total fluids in Figs. 2 and 4 suggest that NMR measures the same bound hydrocarbon porosity as TRA. One explanation may be that TRA leaves behind a graphite or coke residue from retorting, which also underestimates the bound hydrocarbon porosity. The presence of bitumen with short T_2 and large T_1/T_2 ratio is supported by the observed core-NMR temperature dependence.

The workflow for calibrating core-NMR fluids $\varphi_{\mathrm{CoreNMR1}}$ from the TRA data fluids in Eq. (3) is as follows: (1) the map is plotted as T_1/T_2 ratio (y-axis) vs. T_2 (x-axis), (2) the $(T_1/T_2)_{\mathrm{cutoff}}$ line is fixed to 1 at the maximum T_2 value $T_{2,\mathrm{max}}$ = 1000 ms, (3) the slope of the $(T_1/T_2)_{\mathrm{cutoff}}$ line is adjusted by varying the $(T_1/T_2)_{\mathrm{cutoff}}$ at the minimum T_2 value $T_{2,\mathrm{min}}$ = 0.01 ms such that the integral of the signal in the upper half matches $\varphi_{\mathrm{o2}} + \varphi_{\mathrm{o3}}$, (4) $T_{2,\mathrm{cutoff\text{-}oil}}$ for oil is adjusted so that the signal above $T_2 > T_{2,\mathrm{cutoff\text{-}oil}}$ (and above the $(T_1/T_2)_{\mathrm{cutoff}}$) matches φ_{o2}, and (5) $T_{2,\mathrm{cutoff\text{-}water}}$ for water is adjusted so that the signal above $T_2 > T_{2,\mathrm{cutoff\text{-}water}}$ (and below the $(T_1/T_2)_{\mathrm{cutoff}}$) matches $\varphi_{\mathrm{w1+w2}}$. The matching process is done numerically by minimizing the residual at each of the above stages, in a similar fashion to what was done in Eqs. (5) and (6).

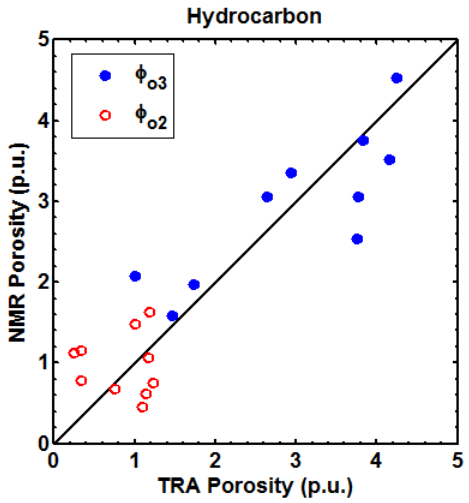

Fig. 5: Correlation cross-plot of the core-NMR hydrocarbon porosity at 100 °C versus the TRA bound hydrocarbon φ_{o3} (filled blue) and TRA total oil φ_{o2} (open red), where TRA is used to calibrate core-NMR (Table 2). The correlation is: R^2 = **0.69** and p = **0.003** for φ_{o3}; no correlation for φ_{o2}, though averages agree.

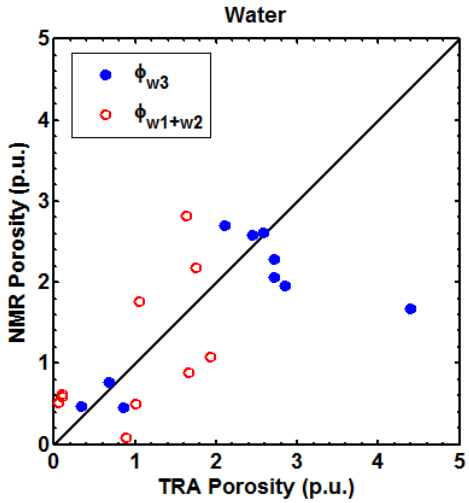

Fig. 6: Correlation cross-plot of the core-NMR water porosity at 100 °C versus the TRA structural clay-bound water φ_{w3} (filled blue) and total water φ_{w1+w2} (open red), where TRA is used to calibrate core-NMR (Table 2). The correlation is: R^2 = **0.44** and p = **0.038** for φ_{w3}; R^2 = **0.34** and p = **0.077** for φ_{w1+w2}.

The calibration parameters are listed in Table 2 as a function of sample temperature during the core-NMR measurement. Figs. 5 and 6 show the resulting correlation between the calibrated core-NMR porosities at 100 °C and the TRA fluid porosities. The calibration of the hydrocarbon phase in Fig. 5 shows higher overall correlation than the water phase in Fig. 6. This is most likely due to the fact that there is more experimental uncertainty for water where T_1 and T_2 are both short. A representative example of T_1/T_2 vs. T_2 correlation maps and calibrated cutoffs are shown in Fig. 7.

Sample Temperature	$(T_1/T_2)_{cutoff}$ @ $T_{2,max}$	$(T_1/T_2)_{cutoff}$ @ $T_{2,min}$	$T_{2,cutoff-water}$ $\varphi_{w3}\|\varphi_{w1+w2}$	$T_{2,cutoff-oil}$ $\varphi_{o3}\|\varphi_{o2}$
Ambient	1	22.0	0.5 ms	2.5 ms
100 °C	1	18.5	0.9 ms	5.0 ms

Table 2: List of core-NMR T_1-T_2 cutoff parameters calibrated from the TRA fluid porosities, as a function of sample temperature during the core-NMR measurement.

TEMPERATURE DEPENDENCE

More information about the nature of the fluids can be obtained by investigating the temperature dependence of each fluid type separately. The first observation from the data in Fig. 7 is that the overall liquid porosity increased by ~1.1 p.u. when heating from ambient to 100 °C. This is due to the fact that, in general, the NMR relaxation times increase with increasing temperature. This is the case for viscous hydrocarbon or bitumen where relaxation times increase significantly with temperature. The effect of increasing relaxation times is to shift signal with short T_2 into the observation window of the NMR

experiment, where the observation window depends on the experimental pulse-parameter T_E = 0.2 ms. The most prominent difference in Fig. 8 is the emergence of porosity in φ_{o3} (bound hydrocarbon quadrant), which is consistent with a heavy-oil signature with short T_2 and large T_1/T_2 ratio [13]. This is an indication that more bitumen signal is entering the observation window upon heating, and that there is most likely additional bitumen signal not being measured.

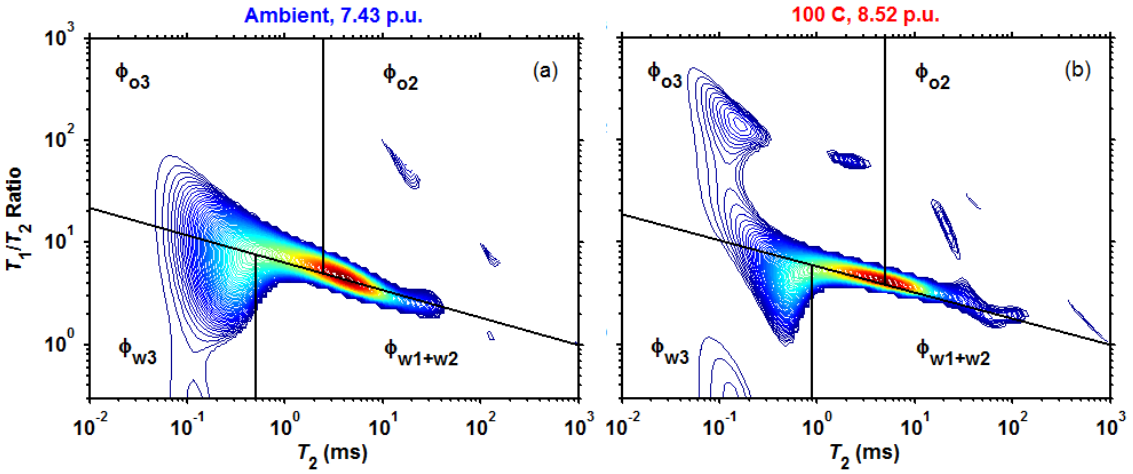

Fig. 7: Representative example of T_1/T_2 vs. T_2 core-NMR correlation map (including cutoffs calibrated from the TRA fluid porosities) as a function of sample temperature (a) ambient and (b) 100 °C during the core-NMR measurement. Porosity (i.e. signal amplitude) is coming out of the page. Quadrants are labelled by TRA fluid, and total liquid porosity is listed in the title. Signal amplitude below $T_1/T_2 < 1$ is a result of broadening from experimental uncertainty.

The second observation in Fig. 7 is that the majority of the signal shifts to the right along the $(T_1/T_2)_{cutoff}$ line with increasing temperature. This temperature shift is quantified by the calibration parameters in Table 2, where $(T_1/T_2)_{cutoff}$ is found to stay roughly constant while the $T_{2cutoff}$ for both oil and water increases by a factor of 2. The temperature dependence of the individual fluid types is shown in Fig. 8.

In order to interpret these data, the origin of the observed T_1 and T_2 must be understood. The observed T_1 and T_2 relaxation times are dominated by either bulk relaxation or surface relaxation, while the diffusion term $T_{2diffusion}$ is negligible for both core and log data [5,6]. In the case of the water phases (φ_{w1+w2} and φ_{w3}), the bulk relaxation terms T_{1bulk} and T_{2bulk} are ≥1000 ms, which are much larger than any observed values. As such, the observed T_1 and T_2 for the water phases are dominated by $T_{1surface}$ and $T_{2surface}$, respectively. The φ_{o2} hydrocarbon phase is interpreted as effective oil, which consists of capillary-bound light oil. The light oil produced from this well is 42 °API with GOR ≅ 1450 scf/bbl, which places the bulk relaxation terms T_{1bulk} and T_{2bulk} at ≥1000 ms. These bulk relaxation times are much larger than any observed values. As such, the observed T_1 and T_2 for the φ_{o2} hydrocarbon phase are dominated by $T_{1surface}$ and $T_{2surface}$, respectively. These observations imply that φ_{o2} porosity is all oil-wet while φ_{w1+w2} and φ_{w3} porosities are all water-wet, indicating no floating fluid pockets inside the pore space. Finally, the φ_{o3} hydrocarbon phase is interpreted as viscous hydrocarbon or bitumen,

which has very short bulk relaxation times. As such, the observed T_1 and T_2 for the φ_{o3} hydrocarbon phase are dominated by T_{1bulk} and T_{2bulk}, respectively.

The first observation in Fig. 8 is the increase in φ_{o3} porosity with temperature. For T_2 relaxation, this is seen as a shift in existing signal to larger T_2 plus the emergence of new signal at short T_2. For T_1 relaxation this is seen as an increase in porosity at the largest T_1, indicating large T_1/T_2 ratios, consistent with bitumen. The second observation is that for φ_{o2} porosity, T_2 increases by a factor of ~3.2 while T_1 increases by a factor of ~1.9 with increasing temperature. These observations are made on the right edge of the distributions. The third observation is that for φ_{w3} porosity, T_1 and T_2 both increase by a factor ~1.6 with increasing temperature. These observations are made at the peak of the distributions. The fourth observation is that for φ_{w1+w2} porosity, the mean of the T_1 and T_2 distributions do not change significantly with increasing temperature.

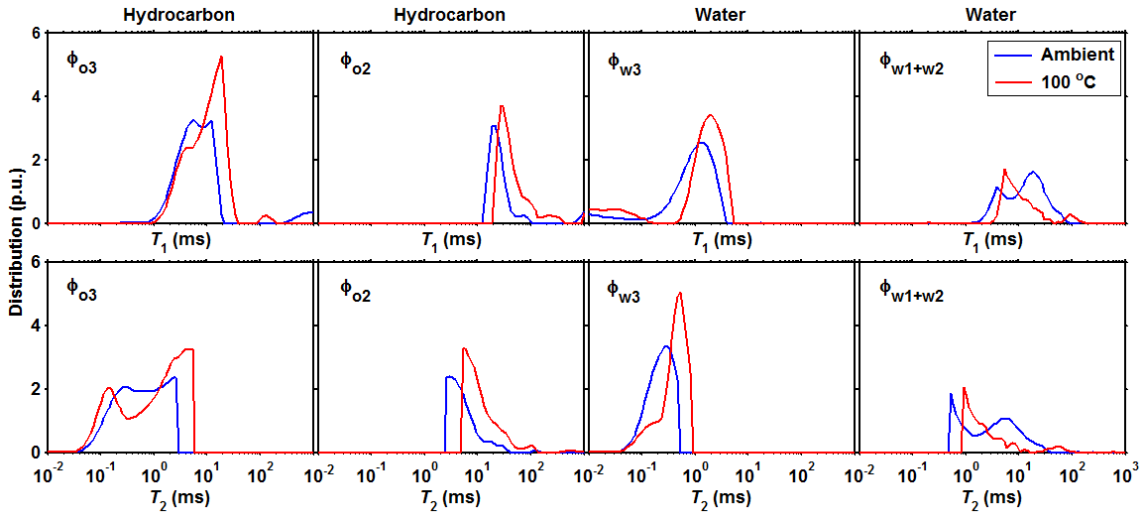

Fig. 8: Core-NMR T_1 projections (top row) and T_2 projections (bottom row) from the representative example in Fig. 7, as a function of sample temperature at ambient (blue) and 100 °C (red) during the core-NMR measurement. Columns correspond to the partitioned quadrants of the core-NMR T_1-T_2 map in Fig. 7. The observed change in φ_{w1+w2} porosity with temperature is a result of scattering (Figs. 5 and 6). Note that φ_{o3} data are most likely dominated by bulk relaxation, while φ_{o2}, φ_{w3}, and φ_{w1+w2} data are most likely dominated by surface relaxation.

The above observations suggest different temperature dependences for all four fluid types. The temperature dependence in φ_{o3} is consistent with bitumen [13]. As discussed in Refs. [5,6], the observed temperature dependence for φ_{o2} and φ_{w3} can be accounted for by surface enhanced hydrogen-hydrogen dipole-dipole relaxation, 2D surface diffusion of wetting molecules in the presence of paramagnetic surface sites, or both. The lack of temperature dependence for φ_{w1+w2} can be accounted for by paramagnetic surface relaxation in the fast diffusion regime.

PORE BODY AND THROAT SIZE

SEM and EDAX indicate that the majority of the samples are fossiliferous, calcareous mudstone. These samples contain high quantities of calcite, both in the form of matrix

cement and biotic fragments (largely foraminifera and disarticulated coccolithophorid algae). The mudstone matrices are composed of calcite cement admixed with moderate quantities of clay minerals (generally less than 30% by visual inspection). Organic matter type varies with discrete particles, lenses, and finely disseminated kerogen is common. The source of the kerogen is from the coccolith microfossils. Kerogen partially coats the disarticulated coccolith plates and lines pore walls, creating predominantly oil-wet surface chemistry.

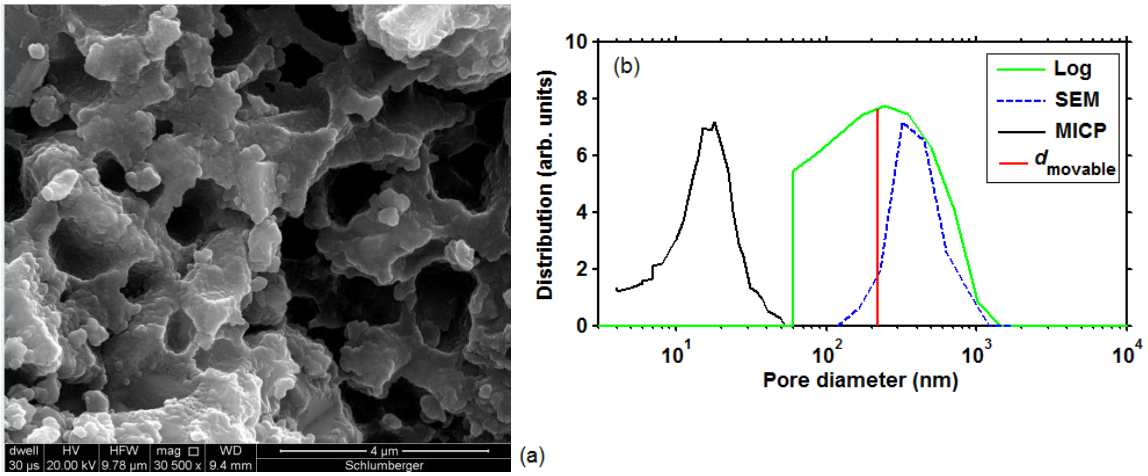

Fig. 9: (a) Representative SEM image (8 µm x 8 µm) of the largest oil-wet IP pores encountered in these organic shale samples. A distribution of the 2D pore-body diameters is extracted from similar images and is displayed in (b) in blue. (b) Log-NMR T_2 distribution (green) converted to pore-body diameter by matching to the right edge of the SEM (dashed blue). Only the effective porosity (> 63 nm) portion of the log-NMR data is shown. Also shown is the pore-throat distribution from MICP (black), indicating a body-throat ratio in the range of 15 ⇔ 30. Red line is the pore-body cutoff ($d_{movable}$ = 219 nm) for movable oil in oil-wet IP pores, calibrated from core-NMR data.

A representative SEM image of the largest IP pores encountered is shown in Fig. 9a. These large pores are interpreted as degraded remnants of bitumen, and constitute oil-wet IP pores. The 2D pore-body sizes are extracted visually from the image [6], and a statistical distribution of the 30 largest pore-body diameters is shown in Fig. 9b. The largest pore-body diameter is ~1000 nm. Also shown in Fig. 9b is the log-NMR T_2 distribution converted to pore-body size. The conversion from T_2 to pore-body diameter (d_{body}) is $d_{\mathrm{body}} = 6\,\rho_{2o} T_2$ (assuming spherical pore geometry) or $d_{\mathrm{body}} = 4\,\rho_{2o} T_2$ (assuming cylindrical pore geometry). The surface-relaxivity parameter ρ_{2o} for large oil-wet IP pores is calibrated by matching the right edge of the log-NMR distribution to the right edge of the SEM pore-body distribution. The data indicates ρ_{2o} = 4.4 µm/s (spherical pores) or ρ_{2o} = 6.6 µm/s (cylindrical pores), which is a consistent range with conventional carbonate rocks. Table 1 lists the various pore diameter cutoffs, which are independent of the assumptions in pore geometry.

Log-NMR pore-body diameters < 63 nm are not interpreted as pores since this region is dominated by viscosity effects of the hydrocarbon phase, therefore only the effective porosity > 63 nm is shown in Fig. 9b. The movable fluid region > 219 nm is signal from

movable oil in large oil-wet IP pores. One assumption is that ρ_{2o} for oil in oil-wet IP pores is the same as ρ_{2w} for water in water-wet IP pores, which may not be the case [10]. Elemental log analysis indicates that the majority of the movable fluid is oil, and SEM data indicates that all the large pores are oil-wet similar to Fig. 9a. The pore-body distribution > 219 nm is therefore the most accurate region for interpretation.

The MICP data can also be used to estimate the matrix permeability to gas. Assuming a simple model of winding, non-intersecting tubes of radius r, the permeability is given by $K = r^2/8F$. The formation factor is $F = a/\varphi^m$, where a = 1 and m = 2 are assumed. The gas pressure-decay permeability is measured on as received crushed sample [14], therefore the relevant porosity is φ_g. Using the pore-throat entry diameter from MICP, which is typically d_{entry} ~40 nm (Fig. 9b), a matrix permeability model K_{entry} is proposed in Eq. (7) below. The comparison between the K_{entry} model and the measured TRA permeability is shown in Fig. 10.

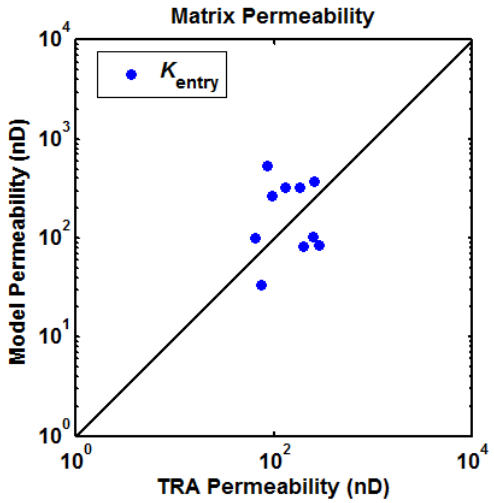

Fig. 10: Cross-plot of the matrix permeability model in Eq. (7) versus the TRA gas permeability on crushed core sample.

There is no correlation in the data, however, it is remarkable that the log-mean average from the model K_{entry} ~160 nD is so close to the measured log-mean average TRA permeability ~140 nD.

$$K_{entry} = \varphi_g^2 \, d_{entry}^2 \, /32 \tag{7}$$

A broader permeability range is under investigation to test for a possible correlation.

CONCLUSIONS

Techniques are described for calibrating NMR log interpretation with core data in organic shale reservoirs. The calibrated NMR log parameters in organic shale are significantly different from conventional rock types, which highlights the importance of core analysis in obtaining accurate reserves and target zone identification in unconventional plays. Techniques are described for partitioning core-NMR T_1-T_2 maps into hydrocarbon and water phases by calibrating the core-NMR data with core porosity data. The natural extension is to apply this technique to down-hole NMR logs for saturation logging. The temperature dependence of the core-NMR response is investigated on the water and hydrocarbon phases separately. The data reveals a significant temperature effect on T_1 and T_2 for the light hydrocarbon phase in oil-wet IP pores, which cannot be explained with conventional surface paramagnetism. The NMR pore-size distribution is calibrated with SEM images, indicating that the majority of the oil is produced from oil-wet IP pores > 219 nm. A matrix permeability model based on the MICP pore-throat entry diameter is proposed which agrees well with the overall magnitude of the core data.

ADCKNOWLEDGEMENTS

The authors would like to thank Matador Resources Company and Schlumberger for allowing the publication of this work. The authors acknowledge Leslie Zhang and George Assad for the MICP measurements, and John F. Keller for the TRA measurements.

REFERENCES

1. Coope D.F., Quinn T.H., Frost E., Manning M.J., "A Rock Model for Shale Gas and its Application Using Magnetic Resonance and Conventional LWD Logs", SPWLA, (2009), 23168.
2. Bray J., Smith C.H., Ramakrishna S., Menendez E., "Magnetic Resonance Utilization as an Unconventional Reservoir Permeability Indicator", SPE, (2011), 145709.
3. Hook P., Fairhurst D., Rylander E., Badry R., Bachman N.H., Crary S., "Improved Precision Magnetic Resonance, Acquisition: Application to Shale Evaluation", SPE, (2011), 146883.
4. Cao Minh C., Crary S., Zielinski L., Liu C.B., Jones S., Jacobsen S., "2D-NMR Applications in Unconventional Reservoirs", SPE, (2012), 161578.
5. Rylander E., Singer P.M., Jiang T., Lewis R.E., McLin R., Sinclair S.M., "NMR T_2 Distributions in the Eagle Ford Shale: Reflections on Pore Size", SPE, (2013), 164554.
6. Jiang T., Rylander E., Singer P.M., Lewis R.E., Sinclair S.M., "Integrated Petrophysical Interpretation of Eagle Ford Shale with 1-D and 2-D Nuclear Magnetic Resonance (NMR)", SPWLA, (2013), New Orleans, USA.
7. Sigal R.F., Odusina E., "Laboratory NMR Measurements on Methane Saturated Barnett Shale Samples", *Petrophysics*, (2011), **52** no. 1, pp. 32-49.
8. Kausik R., Cao Minh C., Zielinski L., Vissapragada B., Akkurt R., Song Y.-Q., Liu C., Jones S., Blair E., "Characterization of Gas Dynamics in Kerogen Nanopores by NMR", SPE, (2011), 147184.
9. Odusina E., Sondergeld C., Rai C., "An NMR Study of Shale Wettability", SPE, (2011), 147371.
10. Ozen A.E., Sigal R.F., "T_1/T_2 NMR Surface Relaxation Ratio for Hydrocarbons and Brines in Contact with Mature Organic-Shale Reservoir Rocks", *Petrophysics*, (2013), **54** no. 1, pp. 11-19.
11. Handwerger D.A., Suarez-Rivera R., Vaughn K.I., Keller J.F., "Improved Petrophysical Core Measurements on Tight Shale Reservoirs Using Retort and Crushed Samples", SPE, (2011), 147456.
12. Loucks R.G., Reed R.M., Ruppel S.C., Hammes U., "Spectrum of Pore Types and Networks in Mudrocks and a Descriptive Classification for Matrix-related Mudrock Pores", AAPG Bulletin, (2012), **96** no. 6, pp. 1071-1098.
13. Yang Z., Hirasaki G.J., Appel M., Reed D.A., "Viscosity Evaluation for NMR Well Logging of Live Heavy Oils", *Petrophysics*, (2012), **53** no. 1, pp. 22-37.
14. Suarez-Rivera R., Chertov M., Willberg D., Green S., Keller J.F., "Understanding Permeability Measurements in Tight Shales Promotes Enhanced Determination of Reservoir Quality", SPE, (2012), 162816.